Microfabrication through Self-Ordering of Cracks: Mechanism, Upscaling and Application for Transparent Electrodes

Fanny Thorimbert, Ambre Brachfeld, Mateusz Odziomek, Cedric Boissiere, Heinz Amenitsch, Denys Naumenko, Giorgio Mattana, Niki Baccile, Marco Faustini

Microfabrication through Self-Ordering of Cracks: Mechanism, Upscaling and Application for Transparent Electrodes

Fanny Thorimbert, Ambre Brachfeld, Mateusz Odziomek, Cédric Boissière, Heinz Amenitsch, Denys Naumenko, Giorgio Mattana, Niki Baccile, and Marco Faustini[*]

F. Thorimbert, A. Brachfeld, C. Boissière, N. Baccile, M. Faustini
Sorbonne Université, CNRS, UMR 7574, Chimie de la Matière Condensée de Paris, F-75005 Paris, France.
marco.faustini@sorbonne-universite.fr

M. Odziomek
Colloid Chemistry Department, Max Planck Institute of Colloids and Interfaces, Am Mühlenberg 1, 14476 Potsdam, Germany.

H. Amenitsch, D. Naumenko
Institut of Inorganic Chemistry, Graz University of Technology, Graz, Austria

G. Mattana
Université Paris Cité, CNRS, UMR 7086, ITODYS, F-75013 Paris, France.

M. Faustini
Institut Universitaire de France.

Keywords: pattern, cracks, colloids, self-assembly

When drying a colloidal solution, cracks appear in the resulting colloidal film. In certain cases, spontaneous order is observed, and cracks form arrays of periodic patterns. Although this phenomenon might be envisioned as a patterning method, overcoming practical challenges is necessary to transform it into a technological tool for microfabrication. This study explores various technological aspects aimed at leveraging the self-assembly of cracks as a scalable microfabrication tool for large-scale device production. Through a series of

analyses, including time-resolved GISAXS, we offer novel insights into controlling the crack self-ordering mechanism, minimizing defects, and implementing strategies for large-scale patterning and pattern transfer. The process proves to be surprisingly robust, maintaining its efficacy with the same colloidal solution even after two years. By introducing biphasic dip-coating, we achieve large-scale crack patterns up to 100 cm^2, while preserving their periodicity and ordering. As a proof of concept, we showcase the use of crack-patterned colloidal films as masks for fabricating metallic sub-micrometer objects, that serve as transparent electrodes with adjustable transparency and conductivity. Overall, this method presents significant advantages over conventional lithography, being cost-effective, versatile, environmentally friendly, and scalable, thereby offering new perspectives for diverse applications requiring cost-effective and large-scale patterning.

1. Introduction

Surface patterning is a key technology to add specific functionalities to thin films. Patterned surfaces find applications in various fields, such as nano- and micro-fluidics,[1] electronics,[2] optics,[3] sensing,[4] photovoltaics,[5] photonics,[6–8] among others. A patterning process is characterized by several features such as resolution, ordering, cost, scalability, versatility, or robustness. The degree of importance of each of those features depends on the targeted applications. For some high-added-value applications, such as electronics or data storage [9,10] the resolution is of utmost importance. In this case, several high resolution patterning technologies such as Extreme UV lithography,[11–13] Nano Imprint Lithography,[14–18] or even Directed Self-Assembly of block-copolymers[19–21] are now well established and even commercialized.[22] For other applications that require patterned surfaces over large areas and at low cost, technological and economic challenges arise. For instance, large scale patterned surfaces can be used to (i) fabricate transparent electrodes[23–25] in smart windows, (ii) to manage heat exchanges, condensation,[1] or boiling[26] (iii) to induce super-wetting properties such as super-hydrophobic, -amphiphobic surfaces,[27] anisotropic,[28] or gradient of wetting properties.[29] Despite their potential, developing low-cost, robust, and scalable patterning methods remains a significant hurdle for the lab-to-market transition. In this regard, patterning methods based on self-assembly approaches (stick-slip,[30,31] wrinkling,[32] colloidal lithography[33]) are very promising but they often suffer from limited control, lack of long-range ordering or they are not robust enough to be reproduced at the industrial scale. Another promising approach involves cracks engineering as patterning method; [34,35] this approach necessitates precise control over crack nucleation and propagation, achieved by prefabricating defects (notches) on the substrate, which concentrate stress.[36] However this method typically relies on lithographic techniques for the initial pre-patterning.

An emerging patterning involves the spontaneous organization of cracks during the evaporation of the solvent. This method. does not require prefabricated defects to direct crack propagation. Under specific conditions, it has been observed that cracks propagate perpendicularly to the evaporation front forming arrays of radial cracks with relatively uniform spacing. This spontaneous ordering of cracks occurs only upon particular drying conditions of colloidal solutions. The origin of the formation of uniform crack patterns upon directional drying of colloidal solution has been described by Allain and Limat.[37] It has been shown that by controlling the evaporation front and the processing parameters, colloidal films

with ordered arrays of radial or linear cracks.[38–40] Several studies describe the influence of some main parameters and indicating general tendencies. However, the previous experiments were carried out on different materials and experimental conditions and the results are sometimes contradictory or vague.[41–46] From a processing point of view, two meniscus-guided techniques, dip-coating and blade coating, have been employed to control crack self-assembly, but this approach has only been applied on a small scale (a few cm^2). Furthermore, the key issues of reproducibility, the presence of defects, and the robustness of the method have not yet been addressed.

The main aim of this work is to take further steps in transforming cracking self-ordering into a scalable technological tool for device fabrication. In particular we tackle three important technological aspects: (i) robustness: understanding the mechanism and the impact of various parameters on defect formation and geometrical control (ii) scalability (iii) applicability: of the crack patterned mask for pattern transfer. More specifically, we used the dip-coating process in the capillary regime by using aqueous suspensions of polystyrene (PS) colloids. We investigated the crack self-assembly mechanism by a set of in situ analysis, including *in situ* GISAXS, and carried out a parametric study to improve the robustness of the patterning process. We introduced a bi-phasic dip-coating-assisted crack patterning to further scale-up the patterning process up to 100 cm^2. At last, to demonstrate the applicability of this simple and straightforward patterning method, the crack patterned films were used as masks to fabricate transparent electrodes on large scale with tunable transparency and electrical properties.

2. Results and discussion

2.1. The process

The overall process consists of the directional drying of an aqueous polystyrene (PS) colloidal suspension as depicted in the experiment shown in **Figure 1**. PS colloids have been chosen because (i) they can be synthesized in large quantities, (ii) their size can be tuned and (iii) previous reports in the literature show that they can form periodic cracks on small scale [38]. The colloidal polystyrene (PS) particles are typically stabilized with a nonionic block copolymer, specifically Pluronic F127, incorporated during the initial synthesis phase.[48] The deposition of colloidal suspension by a meniscus-guided technique, in this case dip-coating, in necessary to control the solvent evaporation rate. The coating was carried out at withdrawal

speeds < 0.1 mm.s^{-1}, in the capillary regime,[47,49] in which the solvent evaporation is faster than the deposition rate. Such regime imposes the directionality of the drying process, with the horizontal drying front following the meniscus. The deposition of the PS layer was performed in a closed chamber at 50 °C, to favor water evaporation. The drying process leads to an increase in internal stresses, resulting in the propagation of periodic cracks in the colloidal films.

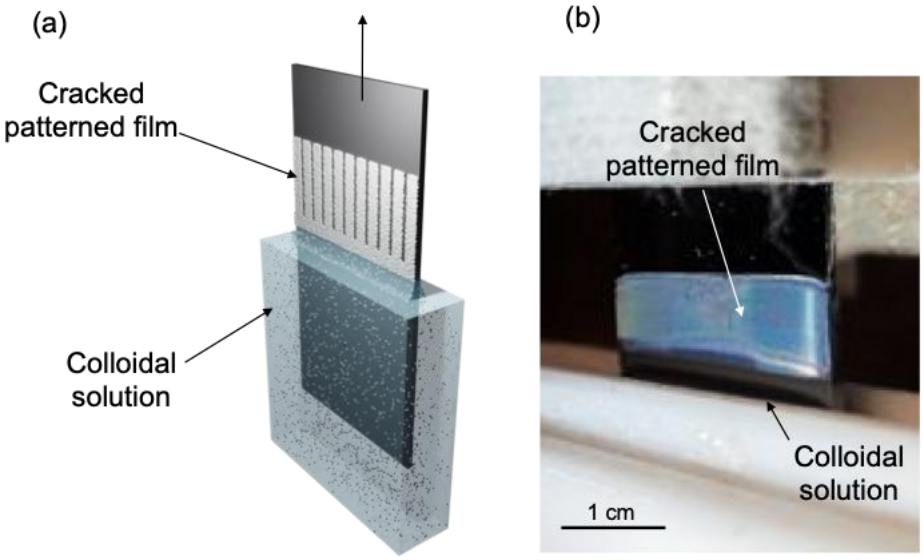

Figure 1: (a) Illustration and (b) photographs of the crack self-ordering process during dip-coating with PS colloids of 70 nm.

The formation of oriented and periodic cracks is visible from a macroscopic point of view as it results in the formation of iridescent colors on the film, due to light diffraction (**Figure 1(b)**).

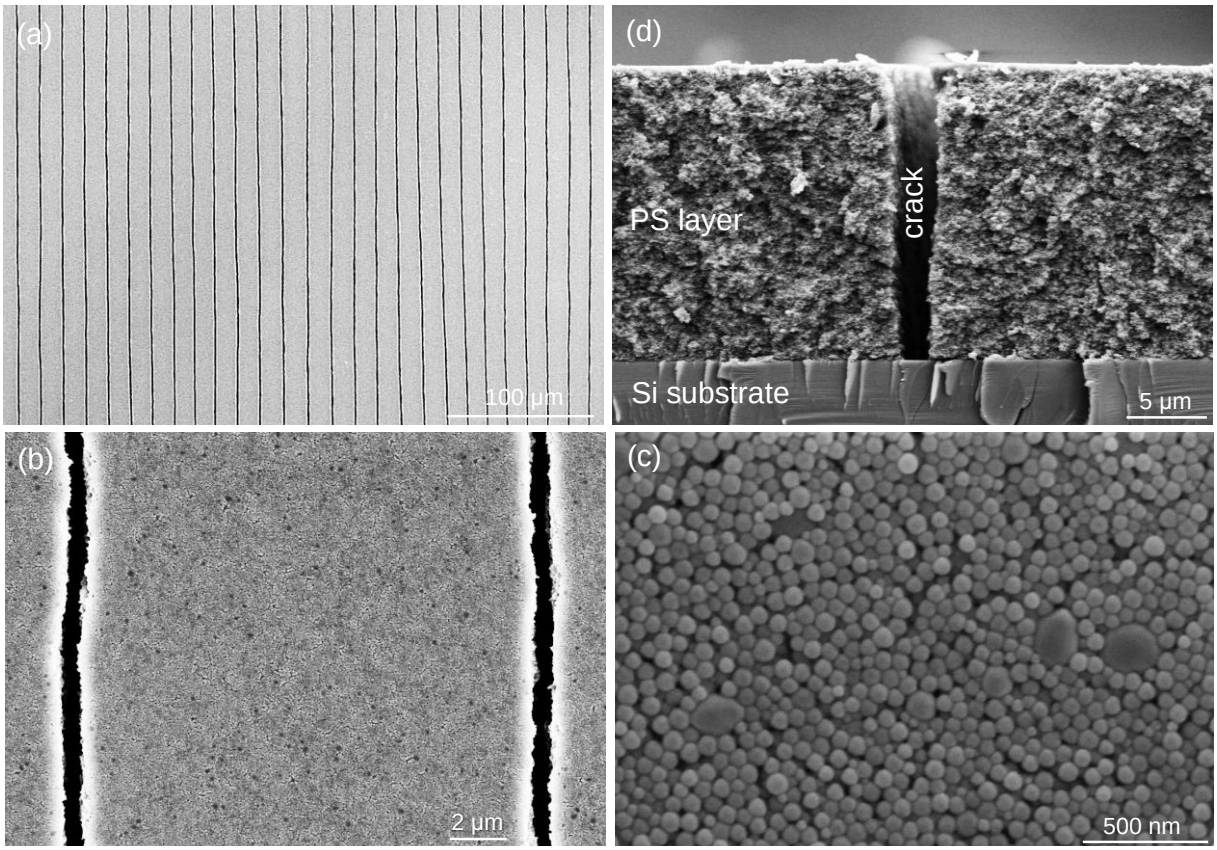

Figure 2: (a-c) Top-view SEM images at different magnifications and (d) cross-section SEM micrograph of the obtained crack pattern.

The cracked PS films were characterized by Scanning Electron Microscopy (SEM) in **Figure 2**. The films present periodic well-aligned cracks (**Figure 2(a) and (b)**) traversing the whole thickness of the film, toward the substrate (**Figure 2(d)**). Looking closer, this multi-layered arrangement film is made of 70 nm colloids (**Figure 2(c)**). While the aforementioned case represents an "ideal" case, among the different parameters that can influence the quality of the final patterns, one of the main parameters is certainly the size of colloids. To unveil the importance of the size of the colloids, we investigated solutions composed of PS colloids with average diameter sizes of 45 nm, 70 nm, and 90 nm (determined by SEM) denoted respectively as PS45, PS70, and PS90. Figure S1 shows the photographs of the colloidal films, SEM micrographs, and the size distribution of each colloidal batch showing a certain polydispersity. The crack patterns obtained from solutions with different colloid sizes are depicted in Figure S2. For the smallest colloid size, as illustrated in Figure S2(a), numerous random horizontal secondary cracks are visible, while for larger particles, regular homogeneous crack patterns are observed in Figure S2(b) and (c). The origin of these random secondary cracks in films obtained with 45 nm colloids was further investigated. The cracking

process was followed by optical microscopy as demonstrated in Figure S2(d). The sequence reveals the oriented periodic cracks form first, succeeded by the appearance of random perpendicular secondary cracks. The quantification of the defects in each system (Figure S3(d)), by image analysis,[50] confirmed the highest density of defects in colloids of smallest size.

Additionally, we studied the influence of particles polydispersity on crack morphologies. For that we prepared a bimodal colloidal system by mixing PS particles of 70 nm with the ones of 45 nm (PS70:PS45), in a 0.25:0.75, 0.5:0.5 and 0.75:0.25 weight ratio. Optical microscopy images of the obtained patterns are presented in Figure S3(e) to (g), while the results of the image analysis are presented in Figure S3(h). Notably, a higher proportion of the smaller 45 nm PS particles consistently led to the formation of numerous secondary cracks. The appearance of perpendicular secondary cracks with 45 nm colloids can be intuitively attributed to a larger capillary pressure arising from a smaller curvature meniscus during drying. The meniscus elastically deforms the particles and generates tensile stress in the film during drying. In films composed of smaller colloids, smaller radius of the meniscus generates larger capillary stress that is relaxed by the opening of additional cracks. This simple study emphasizes that, for this given systems, smaller colloids should be avoided to obtain defect free linear patterns.

However, increasing the colloidal size even more (above 90 nm) does not necessary result in a better self-ordering of cracks. Indeed, dip coating deposition of large colloids is more challenging for two reasons. First, larger colloids are characterized by lower the colloidal stability especially during evaporation leading to less homogenous films. Second, crack patterning in larger colloidal gels is more challenging: it has observed that oppositely to small colloids, during evaporation, larger radius of the meniscus generates lower capillary stress leading to less ordered or even random crack patterns.

2.2 Mechanistic insights: crack arrays nucleation, propagation and drying of the films

After investigating the influence of colloid size distribution on crack-patterning process, we looked at the mechanism of the process. The processes occurring during film deposition (colloidal self-assembly, drying, crack nucleation) were followed by optical microscopy and *in situ* GISAXS. **Figure 3(a)** illustrates the different zones present during crack formation that are observed by optical microscopy image (**Figure 3(b)**). Three distinct zones can be distinguished: the colloidal solution, the colloidal gel (still filled with water), and the dried

colloidal film. They are separated by the "gelification front" and "drying front" respectively. In this configuration, all the periodic cracks appear in the gel part, in a position that we name here the "cracking front".

We also investigated the dynamics of crack propagation by optical microscopy recording a video during the process. **Figure 3(c)** and **(d)** show a time-lapse sequence of micrographs showing the temporal evolution of the system. First, **Figure 3(c)** displays the spatio-temporal evolution of the gelation, cracking, and drying fronts. While the advancement of the gelation front is continuous, the cracking and drying fronts advance step-by-step. This intermittent motion is in agreement with previous reports[51,52] and attributed to the differences between the stresses required to stop and continue a fracture. The characteristic steplike trajectory of the crack front is a direct consequence of the fact that stress for a crack to advance σ_{go} > stress to for a crack to stop σ_{stop}. As the gelation front advances, the stress throughout the film increases over time. A crack will arrest until the local stress exceeds σ_{go}, when it rapidly jumps toward the gelation front before stopping again.[51,52] At first glance, this step-by-step propagation does not seem to have a strong implication on the quality of the final crack arrays. Second, **Figure 3(d)** gives insights into the hydrodynamics of the colloidal deposition, offering an important insight on the deposition mechanism: we highlighted the motion of a dark spot, representing a colloidal aggregate (scattering light) over time. As respect to a previous study concerning the deposition of SiO_2 colloids,[53] in our case the sequence clearly indicates that a capillary flow is responsible for the colloids moving toward the triple points as in the case of the coffee ring effect[54]. This finding is important because it further suggests that thickness of the PS colloidal film applied in the capillary regime is strongly driven by evaporation rate[47]. At last, we investigated the crack nucleation process by observing the top edge of the film. **Figure 3(e)** shows a typical crack-patterned film formed at the very beginning of the dip-coating deposition. The evolution of the pattern geometry from the top to the bottom gives insight on the crack self-ordering process. The micrograph presents three main zones that we attributed to differences in thickness along the vertical direction as we illustrated in the profile in **Figure 3(e)**. From the top to the bottom: (i) a thick deposit close to the edge attributed to "the coffee ring effect" at the very beginning of the dip-coating process; (ii) a thin zone without cracks, probably attributed to fast depinning; (iii) a zone of more homogeneous thickness presenting periodic cracks. The self-ordering of cracks takes place as indicated in the zoomed inset of **Figure 3(e)**: when increasing the thickness, we first observe a transition between disordered cracks toward aligned cracks; then, progressively, when

increasing the thickness some cracks stop which makes the crack arrays highly periodic. This behavior is astonishing since the process is able to "self-correct" initial defects to increase the degree of order during the process.

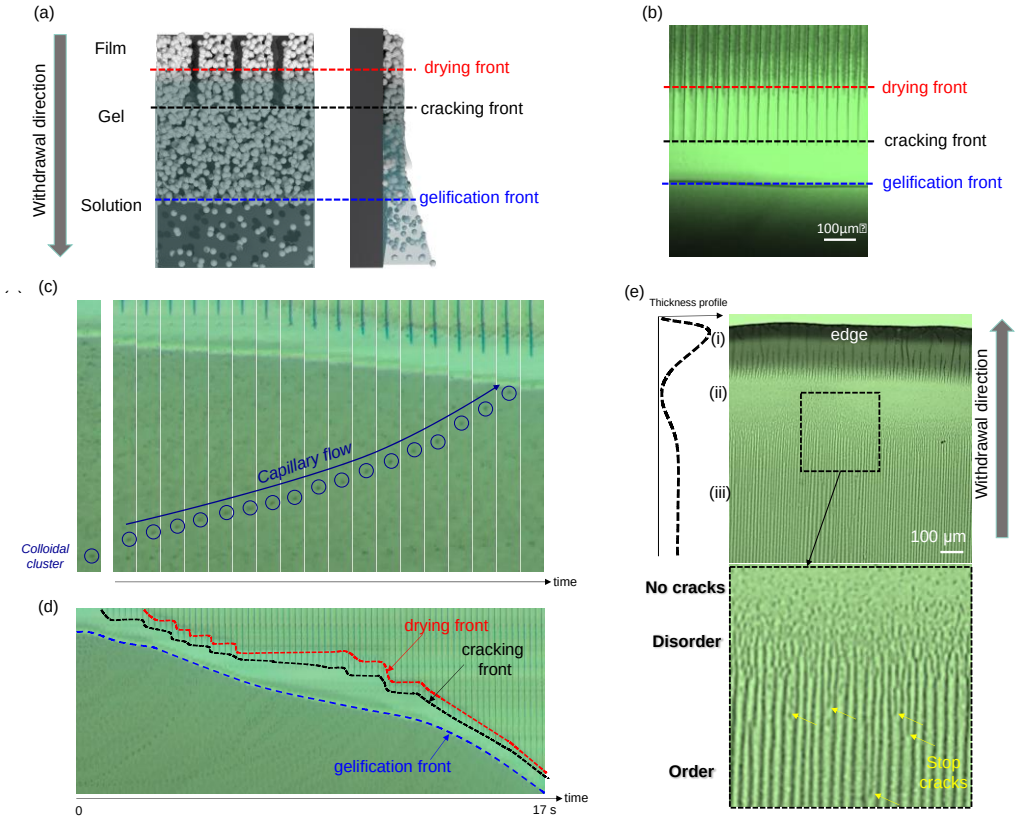

Figure 3: (a) Schematic illustration of the formation of the cracks during dip-coating with (b) the corresponding optical microscopic image (c) and (d) represent micrograph sequences showing the temporal evolution during drying and crack propagation, (e) optical micrographs at the top edge of the sample illustrating the crack arrays nucleation, with a schematical graph representing the thickness profile depending on the deposit position.

We further investigated the drying step, between the gelification and the drying front. To do so, we have designed an experiment based on time-resolved GISAXS during crack formation by dip-coating at low speed; this enables to probe the structural evolution of the colloidal film filled with residual solvent during drying in the zone where the cracks appear and propagate. The experiment was carried out at the SAXS beamline at the Elettra Synchrotron (Italy) and is illustrated in **Figure 4(a)**. The substrate is positioned vertically to perform the dipping of the sample into the solution-containing reservoir. The X-ray beam meets on the sample surface at a fixed angle of incidence (0.2°) adjusted by rotating the sample. The resulting 2D pattern gives insight into the nanoparticle's arrangement. During the *in situ* study the solution moves

vertically, whereas the sample has a stationary position. In addition, a camera is mounted perpendicularly to the sample to see the formation and evolution of cracks. **Figure 4(b)** shows a photograph of the experimental setup with the presence of the X-ray source and the detector, the microscope, the sample, and the solution.

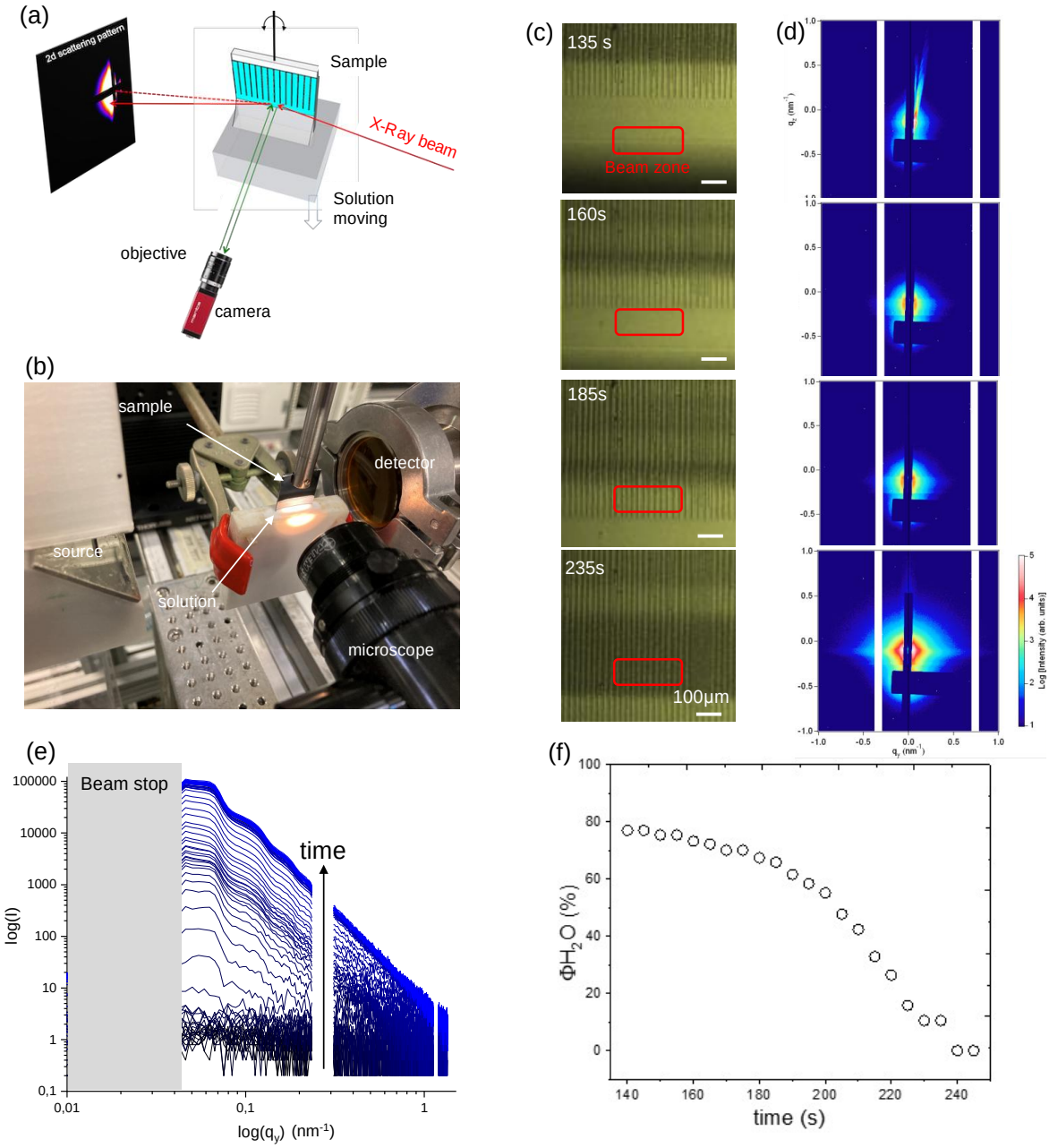

Figure 4: (a) Schematic illustration of the experimental set-up of time-resolved GISAXS, with (b) a photograph of the real experiment. (c) Series of optical microscopic images during the in-situ experiment, with the crack propagation evolution over time, with (d) the corresponding scattered series of images for colloids with a size of 90 nm. (e) Time evolution

of the logarithm of the scattered intensity as function of the logarithm of q_y. (f) Evolution of the volumetric fraction of water in the film as function of time.

We first report the results of the PS colloids of size 90 nm. **Figure 4(c)** represents a selection of optical microscope images at different stages of the process. The zone where the X-ray beams interact with the sample is represented by a red box. Then, the corresponding GISAXS spectra are reported in **Figure 4(d)**. In the first step (t = 135 s), the X-ray beam met the liquid meniscus and we only observed an asymmetric artifact because the surface was not planar. When the film is formed (t > 135 s) a scattering pattern is observed increasing in intensity with time. We integrated the scattered intensity along the q_y direction and we plotted it as function of the time as shown in **Figure 4(e)**. The darkest line represents the first measures (just above the liquid, in the gel part), whereas the brighter blue curves correspond to the last measures obtained on the dried films. First of all, one can observe that the scattering profiles are similar all along the drying process (exception made for the noisy flat data at the beginning of the experiment), the main difference being the scattering intensity which increases in time. A similar behavior was observed for the 70 nm colloidal films as shown in Figure S4(a). We speculate that the increase in intensity is due to the increasing electron density contrast between the polystyrene and the medium, initially water (low contrast) and eventually air (high contrast). To validate this hypothesis, and to gain more insight from the GISAXS *in situ* experiment, we attempted to fit the GISAXS curves **Figure 4(e)** between 140 s (wet film) and 250 s (dry film). Fitting of $I(q_y)$ SAXS curves is classical for colloids in a medium; when the shape and size of the colloids is known, simple sphere, cylindrical or core-shell models can help better understanding the undergoing physicochemical processes. The fit of the SAXS data related to the 90 nm and 70 nm systems was approached with the simplest model possible, a core-shell sphere model (core: polystyrene; shell: F127) with core radius polydispersity and a structure factor involving a hard sphere potential (no electrostatic repulsive interactions involved). The details of the model, as well as the assumption, its limits and typical fits are given in the Supporting Information, Figure S5. The advantage of the present system is that all structural parameters are known (composition and size of colloids), thus limiting the number of free variables (10, **Table in Figure S5(a)**) to a single one, namely the scattering length density (SLD, equivalent to the electron density) of the medium (water, air or a mixture of both). It is then possible to fit all SAXS curves for the 70 nm and 90 nm systems using only the SLD of the medium (selected curves are shown in **Figure S5(b and c)**), which can be correlated to the water content at each time.

The evolution of the water fraction with time for the 90 nm system, shown in **Figure 4(f)**, illustrates the drying process associated to dip-coating, with a marked drop of the water content between 60 % and 0 % after about 200 s. This trend is in good agreement with the optical sequence shown in Figure 4(c) showing the transition between a colloidal gel (filled with water) and a completely dried film. The water content evolution in time associated to the 70 nm system, shown on Figure S4(b), shows similar results at the corresponding time scales observed in the optical microscopy data Figure S4(c). A different approach was on the contrary performed for colloids with a size of 45 nm. As shown in Figure S6(a), the scattering profile for this system presents a steep increase in intensity in the low-q region of the $I(q_y)$ data, thus making the fitting more complex and less reliable. For this reason, we have plotted the slope of the $I(q_y)$ signal below $q= 0.08\ nm^{-1}$ as a function of time (Figure S6 (b)), whereas increase in the scattering intensity at low-q is generally associated with attractive colloidal interactions. The decrease in the slope from 0 to about -4 starting above 800 s can be associated to the compaction of the colloids induced by capillary stresses occurring during complete drying; this change above 800 s also correlates with the appearance of random secondary cracks as determined by image analysis in Figure S6(c). A similar compaction is probably expected to occur for the 70 nm and 90 nm systems, but we speculate that it cannot be observed here when considering the size of the colloids and the available size domain given by the low-q (~150 nm) and high-q (~6 nm) regions.

2.3. Stability of the colloidal suspension

One of the most important requirements to make this approach practically viable concerns the stability over time of the colloidal solution and robustness of the process. To address this, we analyzed the 70 nm PS colloidal solution by dynamic light scattering (DLS). The first measure was taken when the solution was freshly synthesized (Figure S7(a)), whereas the second measure was taken with the same solution two years later (Figure S7(b)). The colloidal solution was stored at room temperature in the laboratory without any special precautions. The average size was initially determined to be equal to 180 nm, and slightly increase up to 240 nm. These values are higher than the average sizes determined by SEM analysis, suggesting that the colloids are slightly aggregated in the solution. However, the slight aggregation had minor influence on the quality of crack patterns as can be seen on Figure S7(c) and (d) prepared from “as prepared” and two-years old solution, respectively. Moreover, the solution was used in between these two years, tens of times and the cracked

samples have comparable patterns, with arrays of cracks highly oriented and periodic even in the case of the solution aged for two years, thus confirming the robustness and the repeatability of the process.

2.4 Geometrical control

Another important aspect concerns the control of the geometrical features of crack-patterned films, such as thickness, crack periodicity, or width of the cracks. According to the literature, crack spacing scales linearly with thickness.[37] Conveniently, in a dip coating process the thickness can be easily tuned by controlling the withdrawal speed; more specifically, in the capillary regime, the thickness is inversely proportional to withdrawal speed.[37,41,47–49]. Consequently, studied the effect of the withdrawal speed for the 70 nm PS colloids. As the withdrawal speed increases from 0.002 to 0.016 $mm.s^{-1}$ both thickness and crack spacing decrease (**Figure 5(a)** and **5(b)**). As shown in **Figure 5(b)** and in the optical micrographs in **Figure 5(d)**, **(e)** and **(f)**, the periodicity of the crack arrays can be tuned from around 40 μm down to less than 10 μm. The limitations of the method need to be mentioned. At ultralow withdrawal speeds ($v < 0.001$ $mm.s^{-1}$), delamination of the film is observed (Figure S8(a)) due to high remaining stress. On the opposite, at higher speeds ($v > 0.018$ $mm.s^{-1}$) the cracks are not ordered anymore (Figure S8(b)). This proves the necessity of a film minimal thickness (made of a multi-layer arrangement of PS particles) required for crack self-ordering. Similarly, we also analyzed the width of cracks by SEM. As shown in **Figure 5(c)** following a similar trend than thickness and periodicity, the width of cracks decreases with the withdrawal speed. Furthermore, to probe a possible effect of the concentration (and thus viscosity) of the colloidal solution we have performed dip-coating deposition by varying the concentration while keeping constant the other processing parameters (Figure S9). The concentration is not influencing the quality of the crack pattern however an increase in the concentration of the colloidal solution results in a thicker film and thus in larger crack spacing (Figure S9).

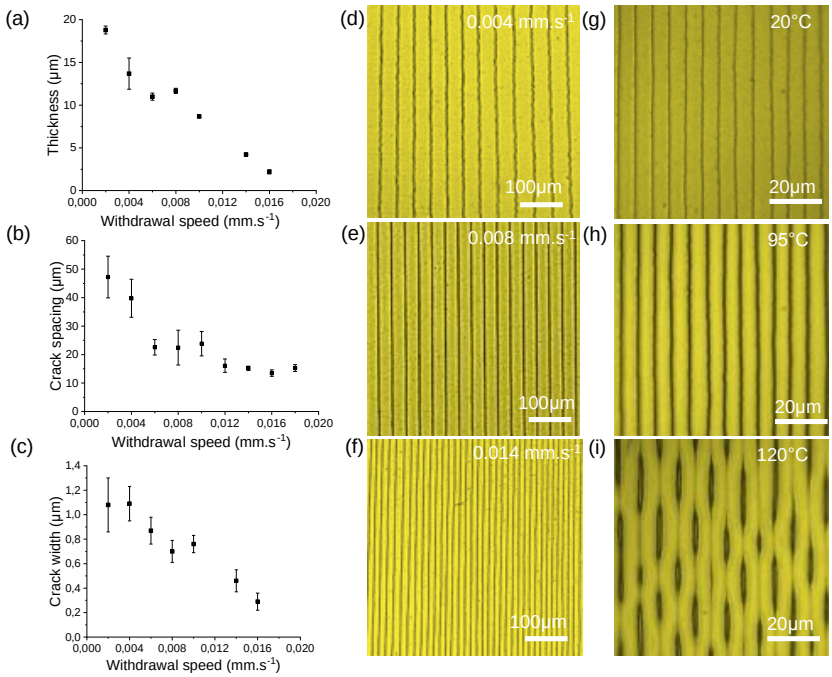

Figure 5: (a) Thickness, (b) crack spacing and (c) crack width as function of the withdrawal speed. Optical microscope images of patterns obtained at (d) v = 0.004 mm.s^{-1}, (e) v = 0.008 mm.s^{-1}, and (f) 0.014 mm.s^{-1}. Optical microscopy and SEM images of PS cracked pattern after dip-coating (g) and after annealing at 95 °C (h) and at 120°C (i).

Taking advantage of the polymeric nature of the colloidal films we attempted to apply a post-thermal treatment to control the width of the cracks by partially melting the PS particles. **Figure 5 (g-i)** reports on the evolution of a crack-patterned layer as function of the temperature. At 20°C, after dip-coating, the average crack's width is equal to 0.57 µm ± 0.05 µm (**Figure 5(g)**), whereas heating the polymer at 95°C results in a crack's width opening to 1.30 µm ± 0.09 µm (**Figure 5(h)**). This can be attributed to a slight shrinkage of the film to due the partial melting of PS particles as shown in SEM images in Figure S10 (a-d). Increasing the temperature further up to 120°C results in further melting and the formation of zig-zag distorted crack patterns as illustrated in **Figure 5(i)** due to the formation of thermally induced capillary instabilities as reported in the literature for other polymeric patterns made by nanoimprint lithography.[55] Moreover, it is also important to notice that the choice of the substrate will influence the deposition of the solution. The substrate plays an important role as in any solution deposition method affecting wetting and adhesion. While the method can be applied to many supports (Si, glass, metals, plastics…),[56] very hydrophobic substrates (like Teflon) often leads to dewetting and/or delamination of the film from the substrate.

To sum up, dip-coating enables a good control of the thickness and crack periodicity through the change in withdrawal speed. The crack width could also be slightly tuned by partial melting through a thermal post-treatment.

2.5. Scaling-up self-ordering of cracks: the biphasic process

Theoretically, dip-coating is a deposition method that can be easily scaled up. Consequently, the self-ordering of cracks could, in principle, be adapted for large-scale patterning. However, the major issue lies in the fact that coating large surfaces requires a significant amount of colloidal solution to fill the tank, which hinders the applicability of this approach. We have implemented a method called here "biphasic dip-coated self-ordering of cracks" by adapting a configuration previously introduced for the deposition of sol-gel inorganic films [57]. The method allows to pattern at a larger scale with a minimum of solution as illustrated in **Figure 6**. In the biphasic method, a large volume of the reservoir is filled by an inert liquid while a small volume of the colloidal solution is added on top of that (**Figure 6(a)**). The bottom inert phase should (i) be denser to be at the bottom part of the reservoir; (ii) be immiscible to prevent the mixing with the colloidal suspension; (iii) present low surface tension to prevent the adhesion of the solution to the substrate. After screening several liquids, we found that methoxy nonafluorobutane meets all the aforementioned requirements as an inert solvent. Above this solvent, approximately 2 cm layer of the PS colloidal solution is added to obtain crack-patterned colloidal films. The main advantage of the biphasic method as respect to the conventional dip-coating method is shown in **Figure 6(b)**, where two samples were obtained from the same amount of PS colloidal solution (16 mL) by dip-coating at 0.008 $mm.s^{-1}$. With such small volume of colloidal solution, only a small sample (of few cm^2) can be coated by conventional dip-coating (Figure 6(b) left side photograph). In contrast the biphasic crack self-ordering method enables patterning a much larger surface up to 50 cm^2 and 100 cm^2 from the same volume of solution as shown in Figure S11 and 6(b) (right side photograph).

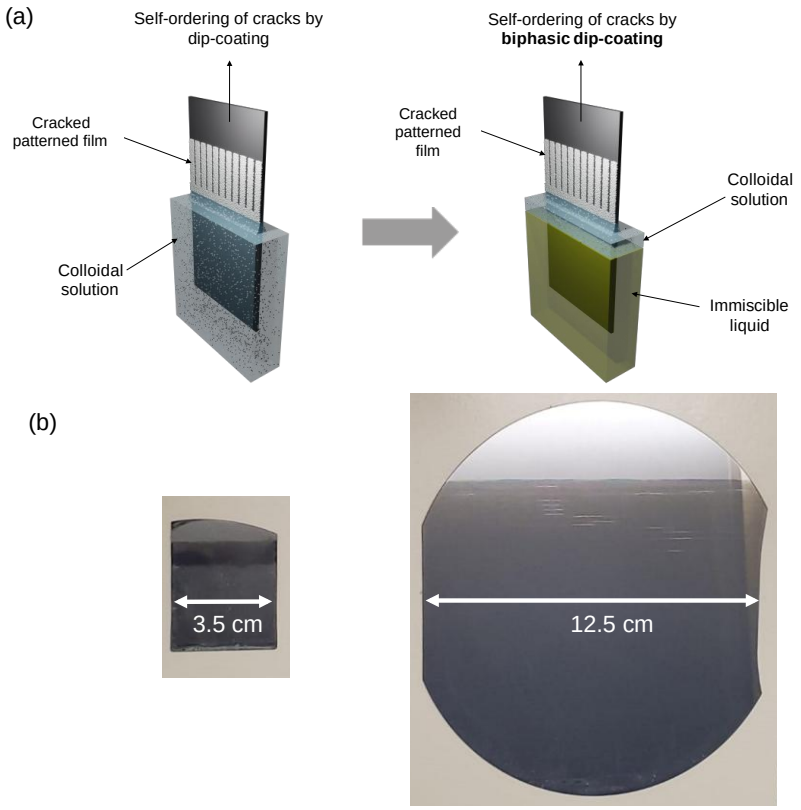

Figure 6: (a) Schematic illustration of the conventional vs biphasic process with the use of a second solvent immiscible and heavier than the colloidal solution. (b) Photography of two samples obtained with 16 mL of colloidal solutions through the conventional and the biphasic method on silicon wafers.

To verify the effectiveness of the biphasic method, we performed a morphological cartography of the 100 cm^2 sample shown on the right of Figure 6(b) to evaluate the eventual presence of defects. More specifically, in **Figure 7(a)** we used a color code to define the nature of the pattern/defects. Four cases can be identified: (i) green regions correspond to periodic oriented arrays of cracks, (ii) yellow regions correspond to local pattern discontinuities due to thickness fluctuation, (iii) red regions are characterized by thinner films with random crack patterns and (iv) blue regions correspond to periodic arrays of cracks with defects of orientation due to edge effect. As shown in **Figure 7(b)**, some random local pattern discontinuities (yellow marks) are present in the middle of the substrate, however, the cartography indicates that the great majority of the surface (except for the borders) is constituted by periodic arrays of oriented cracks. The high quality of the pattern in the green regions was also further confirmed by light diffraction experiments: as shown in Figure S12, in the green regions, the highly periodic crack-patterned PS film act as diffraction grating,

which splits and diffracts light into several beams traveling in different directions when shined by a 532 nm laser beam.

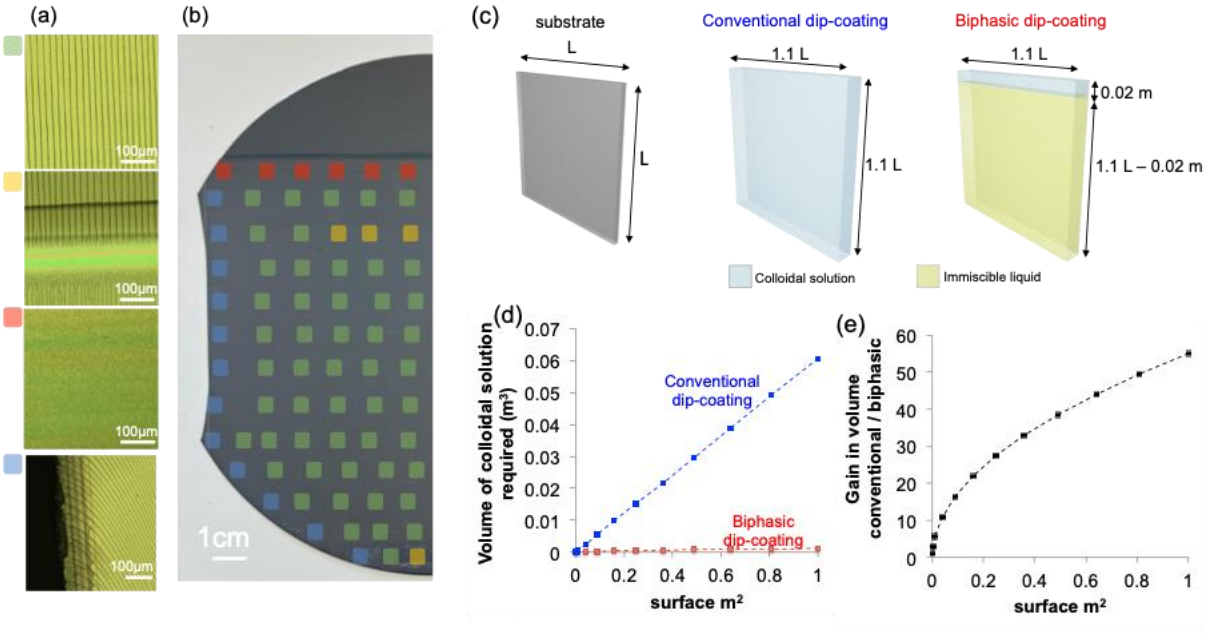

Figure 7: (a) Optical microscopy image of 4 different morphologies observed on the surface The color codes: green = oriented periodic cracks, yellow = discontinuities, red = random cracks, blue = defects of orientation. (b) Cartography of the pattern defects on the 100 cm^2 crack pattern silicon substrate obtained with the biphasic method. (c) Characteristic geometrical parameters to calculate the volume of colloidal solution required to pattern a substrate of size L by conventional and biphasic dip-coating. (d) Evolution of the volume of colloidal solution required as function of the coated surface L^2 for conventional and bi-phasic dip-coating and (e) the gain in volume between the two methods.

In the aforementioned experiment, we demonstrated that surfaces up to 100 cm^2 can be patterned through biphasic-assisted self-ordering of cracks using a minimal amount of solution. Importantly, this method proves to be even more convenient for further scaling up to pattern surfaces at the square meter level. To demonstrate this, we performed a simple upscaling calculation based on the hypothetical case of a square substrate with variable lateral dimensions L, a surface area of L^2, and a constant thickness of 1 cm shown in **Figure 7(c)**. We compare the conventional and the biphasic dip-coating assisted patterning approaches. Based on the calculation detailed in Figure S13, one can evaluate the volume of colloidal solution required for the two methods (**Figure 7(d)**) and the gain in volume of colloidal

solution V_{CS}^{conv} /V_{CS}^{biph} as a function of the substrate surface area L^2. As shown in **Figure 7(e)**, increasing the size of the substrate to be patterned, the gain in volume of colloidal solution increases dramatically. In our configuration, to pattern a 1 m² substrate, the biphasic method requires only 0.0011 m³ of solution, 60 times less than a conventional dip-coating process.

3. Microfabrication of metallic grids as transparent electrodes

At last, we tested the applicability of the PS crack-patterned films to build metallic grids for transparent electrodes with tunable transparency and electrical properties. Metallic nanostructures such as lines or meshes, when applied to transparent substrates like glass or polymeric, enhance the electrical conductivity of the surface without compromising its transparency. [23–25] A common way to fabricate those surfaces involves surface patterning by micro/nanofabrication lithographic techniques and pattern transfer. Films presenting cracks has also been used to prepare transparent electrodes.[58] However, previous examples were based on random network of cracks. By taking advantage of our approach, which enables the easy fabrication of an ordered network of cracks, we explored the microfabrication of gold (Au) grids on glass with various geometries and degrees of ordering. The fabrication scheme to build periodic arrays of Au lines is depicted in **Figure 8(a)**. First the glass substrate was covered by the PS layer with self-ordered cracks, obtained by classical dip-coating, then a 300 nm layer of Au was applied by sputtering over the sample and at last the PS layer was dissolved in acetone to leave arrays of Au lines (**Figure 8(b)**) in the position of the cracks. This was further confirmed in **Figure 8(g)** and **(h)** that display the SEM micrographs of the initial cracked PS layer and the final array of Au lines. In this configuration, the width of Au lines is around 700-800 nm while the spacing between the lines is of 25 µm. Macroscopically the Au lines coated glass are transparent (**Figure 8(e)**) and the process can be easily scaled up to prepare arrays of Au lines on a 65 cm^2 surface by biphasic method as shown in **Figure 8(f)** and Figure S14. The approach can be further extended to fabricate an Au squared grid by repeating the same process starting from a sample covered by Au line and turned 90° as illustrated in **Figure 8(c)** and **Figure 8(d)**. The micrograph in Figure S15 proves that repeating the withdrawal process on gold lines, do not damage the gold electrodes. We then investigated the effect of the geometry on the optical and electrical properties of the samples. As shown in **Figure 8(i)** we first investigated the transmittance of three metallic grids on glass with different geometries named (A) for the Au lines, (B) for the Au squared grids and add an

additional sample named (C) corresponding to random Au grids (Figure S16(c)) obtained from a cracked film obtained with small 45 nm colloids as displayed in Figure S2(a). **Figure 8(i)** shows that all the Au covered samples present a high transparency typically >70%. More specifically, compared to bare glass, the transmittance is lower in presence of Au, following the transmittance order (A)>(B)>(C). Similarly, we measured the electrical resistance of the three samples. The I-V curves shown in **Figure 8(j)** indicates that the samples presents relatively low resistance (ten-hundreds of Ω) indicating that surfaces are conductive and act as electrodes. For reference, the glass substrate alone exhibits a much higher sheet resistance of the order of GΩ. The difference in transmittance and resistance are directly related to the surface covered by Au. This direct relationship is displayed in **Figure 8(k)** in which the % transmittance (at 600nm) and resistance of the three samples are plotted as function of the surface coverage determined by image analysis. In the case of sample A, the array of Au lines covers only 3.5% of the surface; in this configuration the transmittance remains higher but the material is less conductive. On the opposite, the higher surface covering (8%) of the sample C constituted by a random Au grid results in more conductive but less transparent surfaces. As expected, the transparency and electrical resistance are closely related and can be easily tuned by controlling the geometry of the pattern. This patterning approach based on self-ordering of cracks can thus be considered as an appealing candidate to fabricate tunable transparent electrodes on large scale by reducing the steps of the microfabrication process. In contrast to conventional lithographic techniques, such as photolithography, cracked films can be made in a single step and used as mask for the fabrication of sub-micrometric-wide metallic nanostructures without the need for sophisticated equipment. Beyond this simple proof of principle, the patterning approach could be easily extended to other metals with even higher electrical conductivity (such as silver).

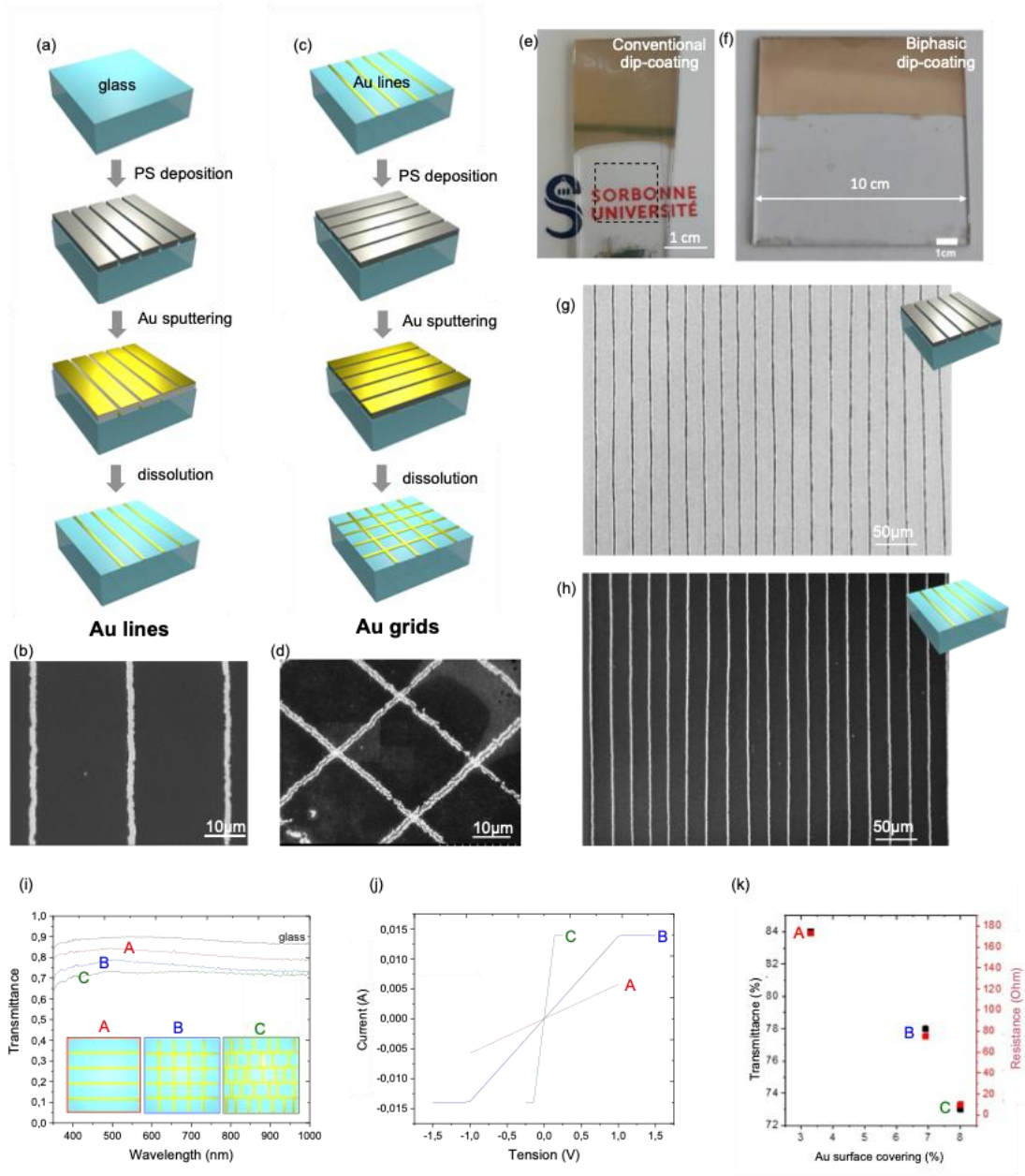

Figure 8: (a) Fabrication scheme and (b) SEM micrograph of the Au lines; (c) fabrication scheme and (d) SEM micrograph Au squared grids. Photographs of the samples covered by Au lines obtained by (e) conventional and (f) biphasic methods. SEM micrographs of (g) the initial PS cracked mask and of (h) the corresponding array of Au lines. (i) Transmittance curves and (j) I-V curves of the three transparent electrodes with different geometries. (k) Relationship between transmittance and resistance as function of the Au surface covering (%) for the three geometries.

4. Conclusion

In conclusion, this study has delved into several technological aspects to transform a "scientific curiosity", the self-assembly of cracks, into a scalable microfabrication tool for device fabrication on large scale. Specifically, compared to previous reports[34,48,49], we offered guidelines to control the process, identify the critical parameters to minimize defects, and introduced strategies for large-scale patterning and pattern transfer. To do so, we first provided further insight into the understanding of the crack self-ordering mechanism and examine the influence of different parameters on defect formation and geometrical control. A series of experiments, such as a time-resolved GISAXS experiment, were conducted to more thoroughly analyze the drying process. We showed that the particle size is responsible of the occurrence of defects, especially for size of colloids below 70 nm. Furthermore, we confirmed that film thickness, crack spacing, and crack width can be easily tuned through the withdrawal speed. Importantly, we have revealed that the patterning process is highly robust and can be replicated with the same colloidal solution, even after two years of aging. We introduced an approach based on biphasic dip-coating, which enables the fabrication of large-scale crack patterns up to 100 cm^2, while preserving crack periodicity and ordering. Finally, we demonstrated the pattern-transfer process and the feasibility of using the crack-patterned colloidal films as masks to fabricate metallic sub-micrometer objects. As a proof of concept, we fabricated gold lines or grids that can be used as transparent electrodes with tunable transparency and resistance depending on the geometry of the crack patterns. More generally, self-ordering of cracks provides significant benefits over traditional lithographic methods: (i) it is cost-effective and does not require complex equipment, as patterning occurs directly during deposition with industrially viable chemical liquid deposition methods like dip-coating; (ii) the patterning approach is highly versatile enabling straightforward pattern transfer; (iii) in contrast to conventional lithographic resists, the employed colloidal solutions are water-based, environmentally friendly, non-toxic and easily recyclable; (iv) these colloidal solutions are exceptionally stable, and the patterning process is durable and can be replicated even after two years, offering major advantages for the future industrialization; (v) using bi-phasic assisted self-ordering of cracks, patterned surfaces can be created over large areas with a very small quantity of solution, an important technological advantage for further upscaling when targeting the square meters objects. For these reasons, this method opens up realistic possibilities for a variety of applications that require large-scale, low-cost micropatterning. One potential application lies in the realm of optoelectronics and photonics, where crack-patterned surfaces could be used as mask to prepare optical surfaces to enhance light absorption or emission in photovoltaic devices or light-emitting diodes (LEDs). By precisely

controlling the geometry and periodicity of the cracks, the optical properties of these devices could be tailored on large scale. Taking advantage of the fact of their periodicity, the crack-patterned surfaces diffract light and could be employed as high-surface-area photonic platforms for chemical or biological sensing applications. The large surface area and tunable dimensions of the crack patterns could enhance the sensitivity (and maybe selectivity) of the optical sensors. Moreover, the crack-patterned surfaces could find applications for large scale wetting, dew harvesting, microfluidics and lab-on-a-chip systems. Crack-patterned substrates could be harnessed to fabricate microchannels on large surfaces for microfluidic devices, for cell culture or chemical reactions. At the end, the crack patterns could serve as low-cost templates for guiding fluid flow or organizing biological or chemical entities, facilitating precise manipulation and analysis at the microscale.

5. Experimental section/Methods

5.1. Synthesis of PS solution

The synthesis was performed in a 2.5 L jacket glass reactor with an air-tightly connected mechanical stirrer and 4 necks. Briefly, the dissolution of 40 g Pluronic F127 (Sigma Aldrich) in 1600 ml of MiliQ water was followed by the addition of 240 g of styrene monomer (Sigma Aldrich) and 3.46 g of $NaHCO_3$ (Alfa Aesar). The monomer was used as received, without any additional purification. The solution was stirred and flushed with N_2 for 1h in order to remove air. In parallel, the solution of the initiator made of potassium persulfate (3.60 g from Sigma Aldrich) dissolved in an additional 80 ml of water was flushed with N_2 for 30 min. The initiator solution was subsequently added to the monomer solution and stirred and flushed with N_2 for another 20 min. The mechanical stirrer was set throughout the process at 270 rpm. The mechanical stirrer was air-tight connected and a slight N_2 flush was kept over the solution level in order to provide slight overpressure, released by a needle incorporated into the rubber cap of one neck. Then, the temperature of the circulated liquid in the jacket was raised to 90°C (achieving 70°C after 35 min and 90°C after 55 min). From the liquid reached 90°C the reaction was continued for 5 h. After that time the temperature was set to 40°C and all the valves were opened in order to quench the radicals with oxygen. The obtained milky solution was further centrifuged at different speeds and separated from the precipitate. The utilized speeds were consecutive: 1) 4k rpm for 10 min; 2) 7K rpm for 20 min; 3) 8k rpm for 15 min; 4) 10k rpm for 40 min. The final solution was dialyzed with MiliQ water exchanged 6 times

each 12 h. After that stable colloidal solution of PS latex particles was obtained. The solution could be further concentrated to the desired concentration by a rotatory evaporator.

The synthesis of the different PS is similar to the protocol described previously. The following table summarize the precursors quantities.

Table 1 Synthetic parameters for the fabrication of the PS colloids

	PS45	PS70	PS90
F127 (g)	5	40	5
Styrene (g)	13	240	30
H_2O (g)	200	1600	200
$NaHCO_3$ (g)	0.447	3.46	0.460
$K_2S_2O_8$ (g)	0.447 in 15 mL H_2O	3.60 in 80 mL H_2O	0.460 in 15 mL H_2O

5.2. Deposition of colloidal PS solution

The dip-coater (ACEdip®, Solgelway) was equipped with a closed chamber in which the temperature was adjusted by a thermal controller. The substrates used for film deposition (silicon wafer or glass slide) were cleaned with acetone and fixed in the chamber preheated to 50°C (unless denoted differently in the text). The substrate was immersed in the colloidal solution (pre-heated in the chamber) at the constant speed of 2 $mm.s^{-1}$ and withdrawn from the polystyrene suspension at a speed between 0.001 – 0.018 $mm.s^{-1}$. Latex concentration was set at 13 wt%.

After the fabrication of the PS cracked layer, a 300 nm Au layer was metalized over the pattern. The sample was then sonicated in acetone for one minute to remove PS (that served as a mask) and obtain the final gold lines or grids.

5.3. Characterizations

SEM imaging was performed with SU-70 Hitachi FESEM, equipped with a Schottky electron emission gun, obtained by an Inlens SE detector (in column). Optical images were acquired by optical microscope Cytoviva.

Transmittance measurements were measured by an UV−visible variable angle spectroscopic ellipsometer (M2000 Woolam) in trasmission mode with an acquisition time of 10 s.

Grazing Incidence Small Angle X-ray Scattering (GISAXS) analysis was performed at the Austrian SAXS beamline at the ELETTRA synchrotron in Trieste (Italy) at a photon energy of 8 keV.37 The beam size was set to 1x0.2 mm^2 (HxV). SAXS images were collected in grazing incidence (0.236°) using Pilatus 3 1M detector (Dectris AG, Switzerland) at a distance of 1942.3 mm from the sample.

DLS experiments are performed using a Malvern Zetasizer Nano ZS90 (Malvern Instruments Ltd, Worcestershire, UK) equipped with a 4 mW He–Ne laser at a wavelength of 633 nm. Measurements were made at 25 °C with a fixed angle of 90° and three acquisitions per sample.

I-V curves of the Au patterns were acquired using a Keithley Semiconductor Analyzer 4200 in a two-probe configuration. Voltage was varied between -1.5 V and + 1.5 V with steps of + 0.01 V. The distance between the two probes was always kept the same (2 cm) during all the measurements. The overall resistance of the Au patterns was estimated by taking the reciprocal of the slope of the I-V curves (three acquisitions per sample type).

Acknowledgments

This work was supported by the European Research Council (ERC) under European Union's Horizon 2020 Programme (Grant Agreement no. 803220, TEMPORE). We thank D. Montero and the Institut des Matériaux de Paris Centre (IMPC FR2482) for servicing FEGSEM & EDX instrumentation and Sorbonne Université, CNRS and C'Nano projects of the Région Ile-de-France for funding.

References

[1] M. Faustini, A. Cattoni, J. Peron, C. Boissière, P. Ebrard, A. Malchère, P. Steyer, D. Grosso, *ACS Nano* **2018**, *12*, 3243.
[2] A. Cattoni, D. Mailly, O. Dalstein, M. Faustini, G. Seniutinas, B. Rösner, C. David, *Microelectron. Eng.* **2018**, *193*, 18.
[3] M. Faustini, A. Grenier, G. Naudin, R. Li, D. Grosso, *Nanoscale* **2015**, *7*, 19419.
[4] X. Ye, Y. Li, J. Dong, J. Xiao, Y. Ma, L. Qi, *J. Mater. Chem. C* **2013**, *1*, 6112.
[5] A. Barranco, A. Borras, A. R. Gonzalez-Elipe, A. Palmero, *Prog. Mater. Sci.* **2016**, *76*, 59.
[6] M. Schaffner, G. England, M. Kolle, J. Aizenberg, N. Vogel, *Small* **2015**, *11*, 4334.
[7] O. Dalstein, D. R. Ceratti, C. Boissière, D. Grosso, A. Cattoni, M. Faustini, *Adv. Funct. Mater.* **2016**, *26*, 81.
[8] E. S. A. Goerlitzer, R. N. Klupp Taylor, N. Vogel, *Adv. Mater.* **2018**, *30*, DOI 10.1002/adma.201706654.
[9] V. Neu, C. Schulze, M. Faustini, J. Lee, D. Makarov, D. Suess, S.-K. Kim, D. Grosso, L. Schultz, M. Albrecht, *Nanotechnology* **2013**, *24*, 145702.

[10] M. Grobis, C. Schulze, M. Faustini, D. Grosso, O. Hellwig, D. Makarov, M. Albrecht, *Appl. Phys. Lett.* **2011**, *98*, 192504.
[11] A. M. Dattelbaum, M. L. Amweg, Julia. D. Ruiz, L. E. Ecke, A. P. Shreve, A. N. Parikh, *J Phys Chem B* **2005**, 14551.
[12] T. Clark, J. D. Ruiz, H. Fan, C. J. Brinker, B. I. Swanson, A. N. Parikh, *Chem. Mater.* **2000**, *12*, 3879.
[13] F. Stehlin, F. Wieder, A. Spangenberg, J.-M. Le Meins, O. Soppera, *J Mater Chem C* **2014**, *2*, 277.
[14] S. Y. Chou, P. R. Krauss, P. J. Renstrom, *Science* **1996**, *272*, 85.
[15] A. Cattoni, P. Ghenuche, A.-M. Haghiri-Gosnet, D. Decanini, J. Chen, J.-L. Pelouard, S. Collin, *Nano Lett.* **2011**, *11*, 3557.
[16] C. Peroz, V. Chauveau, E. Barthel, E. Søndergård, *Adv. Mater.* **2009**, *21*, 555.
[17] H. Schmid, B. Michel, *Macromolecules* **2000**, *33*, 3042.
[18] T. Bottein, O. Dalstein, M. Putero, A. Cattoni, M. Faustini, M. Abbarchi, D. Grosso, *Nanoscale* **2018**, *10*, 1420.
[19] C. M. Bates, M. J. Maher, D. W. Janes, C. J. Ellison, C. G. Willson, *Macromolecules* **2014**, *47*, 2.
[20] A. Knoll, A. Horvat, K. S. Lyakhova, G. Krausch, G. J. A. Sevink, A. V. Zvelindovsky, R. Magerle, *Phys. Rev. Lett.* **2002**, *89*, DOI 10.1103/PhysRevLett.89.035501.
[21] R. A. Griffiths, A. Williams, C. Oakland, J. Roberts, A. Vijayaraghavan, T. Thomson, *J. Phys. Appl. Phys.* **2013**, *46*, 503001.
[22] H. Liu, G. Zhang, X. Zheng, F. Chen, H. Duan, *Int. J. Extreme Manuf.* **2020**, *2*, 042001.
[23] B. Han, Y. Huang, R. Li, Q. Peng, J. Luo, K. Pei, A. Herczynski, K. Kempa, Z. Ren, J. Gao, *Nat. Commun.* **2014**, *5*, DOI 10.1038/ncomms6674.
[24] P. Bellchambers, C. Henderson, S. Abrahamczyk, S. Choi, J. Lee, R. A. Hatton, *Adv. Mater.* **2023**, *35*, DOI 10.1002/adma.202300166.
[25] B. Han, Q. Peng, R. Li, Q. Rong, Y. Ding, E. M. Akinoglu, X. Wu, X. Wang, X. Lu, Q. Wang, G. Zhou, J.-M. Liu, Z. Ren, M. Giersig, A. Herczynski, K. Kempa, J. Gao, *Nat. Commun.* **2016**, *7*, DOI 10.1038/ncomms12825.
[26] D. Quéré, *Nat. Mater.* **2002**, *1*, 14.
[27] T. Lv, Z. Cheng, D. Zhang, E. Zhang, Q. Zhao, Y. Liu, L. Jiang, *ACS Nano* **2016**, *10*, 9379.
[28] P. Ge, S. Wang, J. Zhang, B. Yang, *Mater. Horiz.* **2020**, *7*, 2566.
[29] S. Lowrey, K. Misiiuk, R. Blaikie, A. Sommers, *Langmuir* **2022**, *38*, 605.
[30] H. Uchiyama, M. Hayashi, H. Kozuka, *RSC Adv.* **2012**, *2*, 467.
[31] J. Gao, S. Semlali, J. Hunel, D. Montero, Y. Battie, D. Gonzalez-Rodriguez, R. Oda, G. L. Drisko, E. Pouget, *Chem. Mater.* **2020**, *32*, 821.
[32] H. Vandeparre, S. Gabriele, F. Brau, C. Gay, K. K. Parker, P. Damman, *Soft Matter* **2010**, *6*, 5751.
[33] Y. Wang, M. Zhang, Y. Lai, L. Chi, *Nano Today* **2018**, *22*, 36.
[34] K. H. Nam, I. H. Park, S. H. Ko, *Nature* **2012**, *485*, 221.
[35] M. Kim, D. Ha, T. Kim, *Nat. Commun.* **2015**, *6*, 1.
[36] M. Kim, D.-J. Kim, D. Ha, T. Kim, *Nanoscale* **2016**, *8*, 9461.
[37] C. Allain, L. Limat, *Phys. Rev. Lett.* **1995**, *74*, 2981.
[38] W. Han, B. Li, Z. Lin, *ACS Nano* **2013**, *7*, 6079.
[39] B. Li, B. Jiang, W. Han, M. He, X. Li, W. Wang, S. W. Hong, M. Byun, S. Lin, Z. Lin, *Angew. Chem. - Int. Ed.* **2017**, *56*, 4554.
[40] S. Pan, H. Zou, A. C. Wang, Z. Wang, J. Yu, C. Lan, Q. Liu, Z. L. Wang, T. Lian, J. Peng, Z. Lin, *Angew. Chem. Int. Ed.* **2020**, *59*, 14942.
[41] W. P. Lee, A. F. Routh, *Langmuir* **2004**, *20*, 9885.
[42] K. B. Singh, M. S. Tirumkudulu, *Phys. Rev. Lett.* **2007**, *98*, DOI 10.1103/PhysRevLett.98.218302.
[43] F. Boulogne, F. Giorgiutti-Dauphiné, L. Pauchard, *Oil Gas Sci. Technol. – Rev. D'IFP Energ. Nouv.* **2014**, *69*, 397.
[44] J. Ma, G. Jing, *Phys. Rev. E* **2012**, *86*, DOI 10.1103/PhysRevE.86.061406.
[45] M. S. Tirumkudulu, W. B. Russel, *Langmuir* **2004**, *20*, 2947.

[46] P. Bourrianne, P. Lilin, G. Sintès, T. Nîrca, G. H. McKinley, I. Bischofberger, *Soft Matter* **2021**, *17*, 8832.
[47] M. Faustini, B. Louis, P. A. Albouy, M. Kuemmel, D. Grosso, *J. Phys. Chem. C* **2010**, *114*, 7637.
[48] M. Odziomek, F. Thorimbert, C. Boissiere, G. L. Drisko, S. Parola, C. Sanchez, M. Faustini, *Adv. Mater.* **2022**, 2204489.
[49] M. Le Berre, Y. Chen, D. Baigl, *Langmuir* **2009**, *25*, 2554.
[50] "Orientation J Plugin," **n.d.**
[51] E. R. Dufresne, E. I. Corwin, N. A. Greenblatt, J. Ashmore, D. Y. Wang, A. D. Dinsmore, J. X. Cheng, X. S. Xie, J. W. Hutchinson, D. A. Weitz, *Phys. Rev. Lett.* **2003**, *91*, DOI 10.1103/PhysRevLett.91.224501.
[52] E. R. Dufresne, D. J. Stark, N. A. Greenblatt, J. X. Cheng, J. W. Hutchinson, L. Mahadevan, D. A. Weitz, *Langmuir* **2006**, 7144.
[53] J. Li, B. Cabane, M. Sztucki, J. Gummel, L. Goehring, *Langmuir* **2012**, *28*, 200.
[54] R. D. Deegan, O. Bakajin, T. F. Dupont, G. Huber, S. R. Nagel, T. A. Witten, *Nature* **1997**, *389*, 827.
[55] K. J. Alvine, Y. Ding, J. F. Douglas, H. W. Ro, B. C. Okerberg, A. Karim, C. L. Soles, *Soft Matter* **2009**, *5*, 2913.
[56] F. Thorimbert, M. Odziomek, D. Chateau, S. Parola, M. Faustini, *Nat. Commun.* **2024**, *15*, 1156.
[57] Davide. R. Ceratti, B. Louis, X. Paquez, M. Faustini, D. Grosso, *Adv. Mater.* **2015**, *27*, 4958.
[58] Q. Peng, S. Li, B. Han, Q. Rong, X. Lu, Q. Wang, M. Zeng, G. Zhou, J. Liu, K. Kempa, J. Gao *Adv. Mater. Technol.***2016**, 1, 1600095